A novel AIF tracking method and comparison of DCE-MRI parameters using individual and population-based AIFs in human breast cancer

You may also be interested in:

Effects of compressed sensing on DCE-MRI
David S Smith, E Brian Welch, Xia Li et al.

Blind AIF estimation in DCE-MRI
Matthias C Schabel, Edward V R DiBella, Randy L Jensen et al.

Use of a reference tissue AIF
M Heisen, X Fan, J Buurman et al.

Monte Carlo Blind Estimation of the AIF in DCE-MRI
Matthias C Schabel, Jacob U Fluckiger and Edward V R DiBella

Tumour capillary input function and pharmacokinetic parameters
P Di Giovanni, T S Ahearn, S I Semple et al.

Uncertainty and bias in SPGR concentration measurements
Matthias C Schabel and Dennis L Parker

A diffusion-compensated model for the analysis of DCE-MRI data: theory, simulations and
experimental results
Jacob U Fluckiger, Mary E Loveless, Stephanie L Barnes et al.

Reference tissue quantification without a Gd-DTPA calibration
Simon Walker-Samuel, Martin O Leach and David J Collins

Breast pharmacokinetic parameter estimation
P Di Giovanni, C A Azlan, T S Ahearn et al.

A novel AIF tracking method and comparison of DCE-MRI parameters using individual and population-based AIFs in human breast cancer

Xia Li[1,2]**, E Brian Welch**[1,2]**, Lori R Arlinghaus**[1,2]**,
A Bapsi Chakravarthy**[3,4]**, Lei Xu**[5]**, Jaime Farley**[3]**, Mary E Loveless**[1,6]**,
Ingrid A Mayer**[3,7]**, Mark C Kelley**[3,8]**, Ingrid M Meszoely**[3,8]**,
Julie A Means-Powell**[3,7]**, Vandana G Abramson**[7]**, Ana M Grau**[3,8]**,
John C Gore**[1,2,3,6,9,10] **and Thomas E Yankeelov**[1,2,3,6,9,11,12]

[1] Institute of Imaging Science, Vanderbilt University, Nashville, Tennessee, USA
[2] Department of Radiology and Radiological Sciences, Vanderbilt University, Nashville, Tennessee, USA
[3] Vanderbilt Ingram Cancer Center, Vanderbilt University, Nashville, Tennessee, USA
[4] Department of Radiation Oncology, Vanderbilt University, Nashville, Tennessee, USA
[5] Department of Biostatistics, Vanderbilt University, Nashville, Tennessee, USA
[6] Department of Biomedical Engineering, Vanderbilt University, Nashville, Tennessee, USA
[7] Department of Medicine, Vanderbilt University, Nashville, Tennessee, USA
[8] Department of Surgery, Vanderbilt University, Nashville, Tennessee, USA
[9] Department of Physics and Astronomy, Vanderbilt University, Nashville, Tennessee, USA
[10] Department of Molecular Physiology and Biophysics, Vanderbilt University, Nashville, Tennessee, USA
[11] Department of Cancer Biology, Vanderbilt University, Nashville, Tennessee, USA

E-mail: thomas.yankeelov@vanderbilt.edu

Abstract

Quantitative analysis of dynamic contrast enhanced magnetic resonance imaging (DCE-MRI) data requires the accurate determination of the arterial input function (AIF). A novel method for obtaining the AIF is presented here and pharmacokinetic parameters derived from individual and population-based AIFs are then compared. A Philips 3.0 T Achieva MR scanner was used to obtain 20 DCE-MRI data sets from ten breast cancer patients prior to and after one cycle of chemotherapy. Using a semi-automated method to estimate the AIF from the axillary artery, we obtain the AIF for each patient, AIF_{ind}, and compute a population-averaged AIF, AIF_{pop}. The extended standard model is used to estimate the physiological parameters using the two types of AIFs. The mean concordance correlation coefficient (CCC) for the AIFs segmented manually and by the proposed AIF tracking approach is 0.96, indicating accurate and automatic tracking of an AIF in DCE-MRI data of the breast is possible. Regarding the kinetic parameters, the CCC values for K^{trans}, v_p

[12] Author to whom any correspondence should be addressed.

and v_e as estimated by AIF_{ind} and AIF_{pop} are 0.65, 0.74 and 0.31, respectively, based on the region of interest analysis. The average CCC values for the voxel-by-voxel analysis are 0.76, 0.84 and 0.68 for K^{trans}, v_p and v_e, respectively. This work indicates that K^{trans} and v_p show good agreement between AIF_{pop} and AIF_{ind} while there is a weak agreement on v_e.

(Some figures in this article are in colour only in the electronic version)

1. Introduction

Dynamic contrast enhanced magnetic resonance imaging (DCE-MRI) involves the serial acquisition of images before, during and after the intravenous injection of a contrast agent (CA) (Choyke *et al* 2003, Yankeelov and Gore 2007). As the CA perfuses into and out of a given voxel, a characteristic signal-intensity time course results which can then be analyzed with an appropriate pharmacokinetic model to yield estimates of physiological parameters related to tissue perfusion and microvascular vessel wall permeability, plasma volume fraction and the extracellular volume fraction. The values of these parameters vary with different pathological states (Yankeelov *et al* 2005, Hayes *et al* 2002, Checkley *et al* 2003, Schabel *et al* 2010), and quantitative analysis of these parameters over time may provide information regarding treatment response (Delille *et al* 2003, Martincich *et al* 2004, Nagashima *et al* 2006, Yankeelov *et al* 2007, Hamstra *et al* 2005).

Most pharmacokinetic models used in the analysis of DCE-MRI data require the accurate determination of the time rate of change of the concentration of the CA in the blood plasma, C_p, which is typically referred to as the arterial input function (AIF). The accuracy of the measured AIF significantly influences the accuracy of the pharmacokinetic parameters extracted by a particular model (Cheng 2008). However, manual estimation of an AIF for each patient can be a difficult and time-consuming process that can result in variability leading to a decrease in both the accuracy and precision of the pharmacokinetic parameters. If the goal of a DCE-MRI study is, for example, assessing the response of tumors to treatment, then the systematic error introduced into the analysis by incorrect AIF characterization may influence the scoring of response. Hence, it is important to develop an automatic and reliable approach to estimate the AIF for DCE-MRI.

There have been several methods suggested for measuring the AIF (Rijpkema *et al* 2001, Chen *et al* 2008, Mouridsen *et al* 2006, Parker *et al* 2006, Parker *et al* 2003). For instance, Parker *et al* (2003, 2006) present a method to extract the AIF from DCE-MRI data from patients with glioma which requires the manual identification of a particular slice. The time course for each voxel is extracted and the voxels which show a peak of CA within 20 s of the bolus arrival time are identified. From this set of curves, voxels showing a concentration maximum within the top 5% are used to construct the AIF. Similarly, Rijpkema *et al* (2001) extract the AIF by calculating the average maximum CA concentration and setting a threshold based on the average concentration. This method is then applied to MR images from patients with different tumors (head–neck region, prostate carcinoma and brain). Chen *et al* (2008) determine the AIF using two stages: detection and segmentation. The voxels with high signal intensities and fast wash-in are detected first, and then the regions of vessels are segmented by detecting cylindrical objects in 3D MR volumes. Here, we propose a simple and effective semi-automatic approach to obtain the AIF from breast DCE-MRI data that are collected in the sagittal plane.

In addition to detecting the AIF, it is also of interest to assess the difference between AIFs measured in an individual with an averaged AIF measured from a limited population. Currently, there are few studies comparing the results of DCE-MRI analysis with a population or individual AIF in either pre-clinical or clinical studies (Parker *et al* 2006, McGrath *et al* 2009, Wang *et al* 2008). To the best of our knowledge, this is the first study that considers this important comparison in breast cancer patients. We use the novel method described above to estimate the AIF for each individual patient and then compute a population-averaged AIF. These AIFs are applied to one common DCE-MRI pharmacokinetic model to compare the physiological parameters returned by each AIF.

2. Materials and methods

2.1. Data acquisition

Data were acquired from ten patients with locally advanced breast cancer who were enrolled in an ongoing clinical trial. The patients provided informed consent and the study was approved by the ethics committee of our cancer center. DCE-MRI was performed using a Philips 3T Achieva MR scanner (Philips Healthcare, Best, The Netherlands). A four-channel receive double-breast coil covering both breasts was used for all imaging (Invivo, Gainesville, FL). Data for a T_1 map were acquired with a 3D gradient echo multi-flip angle approach with a *TR/TE* of 7.9/1.3 ms and ten flip angles ranging from 2 to 20° in 2° increments. The acquisition matrix was $192 \times 192 \times 20$ (full-breast) over a sagittal square field of view (FOV) of 22 cm^2 with a slice thickness of 5 mm, one signal acquisition and a SENSE factor of 2 for an acquisition time of just under 3 min. The dynamic scans used identical parameters and a flip angle of 20°. Each 20-slice set was collected in 16 s at 25 time points for approximately 7 min of scanning. For the DCE study, a catheter placed within an antecubital vein delivered the dose of 0.1 mmol kg^{-1} of the CA gadopentetate dimeglumine, Gd-DTPA, (Magnevist, Wayne, NJ) at 2 mL s^{-1} followed by a saline flush after the acquisition of three baseline dynamic scans. The volume injection was 9–15 mL depending on patient weight. Each patient was scanned prior to and after one cycle of neoadjuvant chemotherapy yielding a total of 20 data sets.

2.2. DCE-MRI data analysis

Pre-contrast T_1 values, T_{10} values, were computed from the multi-flip angle data by fitting to the equation

$$S = S_0 \sin a \frac{1 - \exp(-TR/T_1)}{1 - \cos a \exp(-TR/T_1)}, \tag{1}$$

where α is the flip angle, S_0 is a constant dependent on the scanner gain and proton density, and we assume $TE \ll T_2^*$ so that T_2^* effects are neglected. The fitting routine employs a standard gradient-expansion, nonlinear, least-squares, curve-fitting algorithm written in the Interactive Data Language (Research Systems, Boulder, CO, USA). Voxels for which the fitting algorithm did not converge were set to zero and those voxels were not used in subsequent analyses.

DCE-MRI data were analyzed by the fast exchange limit formalism (Landis *et al* 2000, Yankeelov *et al* 2003). With this assumption, the longitudinal relaxation rate constant, R_1 ($\equiv 1/T_1$), is given by

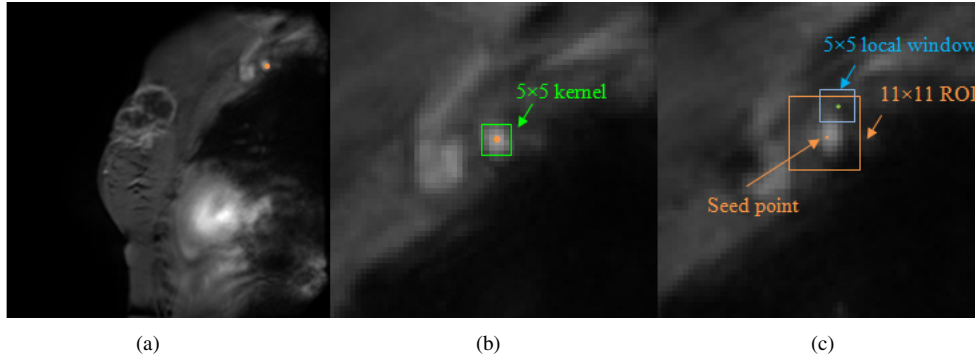$$R_1(t) = r_1 C_t(t) + R_{10}, \tag{2}$$

Figure 1. The voxels contributing to the AIF are selected by first placing a seed point within the axillary artery of a single slice and defining a 5×5 kernel centered on the seed. In a slice adjacent to the one containing the seed, an 11×11 ROI is selected and for each voxel in that ROI, a 5×5 local window centered on that voxel is defined. The CC of the signal-intensity between the kernel and each local window is then calculated. Panel (a) shows the center slice of tumor with the manually selected seed point, while panels (b) and (c) display the zoomed-in ROI with 5×5 kernel centered on the seed point and the zoomed-in 11×11 ROI within the adjacent slice, respectively.

where r_1 is the CA longitudinal relaxivity, R_{10} is the pre-contrast longitudinal relaxation rate constant and C_t is the time course of the concentration of the CA in tissue. To compute C_t, we use the extended standard model that incorporates a plasma term (Yankeelov and Gore 2007):

$$C_t(T) = K^{\text{trans}} \int_0^T C_p(t) \exp(-(K^{\text{trans}}/v_e)(T - t)) \, dt + v_p C_p(T), \qquad (3)$$

where K^{trans} is the CA volume transfer rate constant, v_e is the extravascular–extracellular volume fraction, v_p is the blood plasma volume fraction and $C_p(t)$ is the concentration of the CA in blood plasma (i.e. the AIF).

Data from each DCE-MRI study were fit on a voxel-by-voxel basis with equations (2) and (3) to yield estimates of K^{trans}, v_e and v_p. Similar to the fitting of T_{10}, voxels for which the fitting algorithm did not converge or converged to non-physical values (i.e. $K^{\text{trans}} > 5.0 \, \text{min}^{-1}$, $v_e > 1.0$, $v_p > 1.0$, or below 0.0) were set equal to zero and not used in further analyses. K^{trans}, v_e and v_p parametric maps were generated for each imaging session. Additionally, only voxels that could be fit using both the AIF$_{\text{ind}}$ and AIF$_{\text{pop}}$ were used in the comparison.

2.3. AIF tracking algorithm

For each slice in the image volume, the 25 dynamic scans are averaged; this results in a high signal-to-noise ratio (SNR) data set representing the average intensity over time for each voxel from which it is straightforward to locate the axillary artery. A 5×5 kernel centered on a single, manually selected seed point within the axillary artery in one slice (figures 1(a) and (b)) is then identified. The seed point is selected in the middle of the axillary artery which, depending on individual patient anatomy, is typically located very near the center of the imaging slab between slices 10 and 13. In a slice adjacent to the one containing the seed, an 11×11 region of interest (ROI) is selected automatically and centered on the voxel corresponding to the seed-point location (figure 1(c)). For each voxel in the ROI, a 5×5 'local window' centered on that voxel is defined, and the correlation coefficient (CC) of the signal intensity between the kernel and each local window is calculated. The local window

with the maximum CC is considered as a new kernel and the center point of this kernel is assigned as the new seed point to be used for the next slice. The procedure is repeated for all slices. All voxels yielding the kernels are then used to generate an AIF if they satisfy the following (empirical) criteria:

(1) the $C_p(t)$ maximum must occur within the first three time points post-contrast injection;
(2) the $C_p(t)$ maximum is 20 times greater than the standard deviation of $C_p(t)$ of the first three frames and
(3) the mean $C_p(t)$ of the last ten frames is less than 40% of the maximum $C_p(t)$.

The peaks of each signal-intensity time course satisfying the above criteria are aligned, and the individual AIF is generated through averaging all aligned AIFs. The process is repeated for each patient.

To validate the ability of the proposed AIF tracking algorithm to accurately segment the artery and generate an AIF, the proposed AIF tracking method is compared with a manual detection scheme. During the manual method, the artery is visually outlined (i.e. segmented), and the AIF is generated from the outlined voxels with and without applying the above criteria for each data set. The percentage of voxels that met the criteria is also calculated.

To illustrate how the proposed AIF tracking method rejects voxels that do not exhibit AIF characteristics, including voxels suffering from partial volume effects, a qualitative comparison is performed among the AIFs estimated by (a) outlining the axillary artery manually, (b) outlining the axillary artery manually and filtered by the above criteria and (c) the proposed AIF tracking method. The AIFs obtained by the AIF tracking method and manually with the criteria are also compared quantitatively, through computing the CC and the concordance correlation coefficient (CCC) between them (Lin 1989). The CCC measures the absolute agreement between AIFs; thus, a CCC value of 1 indicates a perfect correlation between AIFs, while a CCC value of 0 suggests completely independent AIFs.

The sensitivity of the AIF tracking method to the assignment of the criteria parameters is also detected through changing the parameters in the criteria by $\pm 15\%$ and comparing the CC between the AIF obtained using the original and changed parameters.

2.4. Comparison of individual and population AIFs

The population AIF is obtained through averaging all 16 individual AIFs. The influence of using the individual and population AIFs are evaluated by fitting the tissue signals to the extended standard model (equation (3)). Both ROI and voxel-by-voxel analyses are performed. For the ROI analysis, the tumor contours are extracted manually in the central slice for each data set first. The signal time courses from voxels in the ROI are averaged and input into the extended standard model to obtain pharmacokinetic parameters. For the voxel analysis, all available voxels within all slices for which the tumor is present are selected, and multiple ROIs are drawn if it is multi-focal disease. Instead of using the averaged signal time course, the signal time course from each tumor voxel is used to compute the R_1. Both the ROI and voxel analyses produce two sets of three parameters:

(1) $K^{\text{trans,ind}}$, $v_{e,\text{ind}}$, $v_{p,\text{ind}}$, using AIF_{ind};
(2) $K^{\text{trans,pop}}$, $v_{e,\text{pop}}$, $v_{p,\text{pop}}$, using AIF_{pop}.

Four statistical methods are employed to compare each pair of parameters (e.g. $K^{\text{trans,ind}}$ and $K^{\text{trans,pop}}$) for both the ROI and voxel-wise analyses: the absolute agreement between the parameter pairs is assessed using the CCC. Here, the CCC evaluates the degree to which these pairs fall on the $45°$ line through the origin. The CC is calculated to measure how far each pair deviates from the best-fit line. Linear regression is performed to calculate the slopes and

the corresponding intercepts. The ratio between parameters estimated by the AIF_{pop} and the AIF_{ind} is also calculated.

Efforts are also made to determine how a difference between the population and individual AIFs would lead to a difference in pharmacokinetic parameters. To explain differences in K^{trans}, the difference in the area under the curve (AUC) from time points 1–8 (0–128 s) is computed for both AIFs for a given patient. Those values are then compared with the slope returned when the population AIF-based K^{trans} are regressed onto the individual AIF-based K^{trans}. It is hypothesized that if the wash-in AUC of the individual AIF is greater than the wash-in AUC of the population AIF, then the K^{trans} values returned from the population AIF would be greater in magnitude than those returned from the individual AIF analysis. In symbols, this reads as

$$AUC_{ind}(0\,s, 128\,s) > AUC_{pop}(0\,s, 128\,s) \Rightarrow K^{trans,pop} > K^{trans,ind}. \quad (4)$$

The same hypothesis is also applied to v_p:

$$AUC_{ind}(0\,s, 128\,s) > AUC_{pop}(0\,s, 128\,s) \Rightarrow v_{p,pop} > v_{p,ind}. \quad (5)$$

To explain the differences in v_e, the area under the wash-out portion of the population and individual AIFs from time points 12–25 (177–400 s) is computed. It is hypothesized that if the wash-out AUC of the individual AIF is greater than the wash-out AUC of the population AIF, then the v_e value returned from the population AIF would be greater in magnitude than those returned from the individual AIF analysis. In symbols, this reads as

$$AUC_{ind}(177\,s, 400\,s) > AUC_{pop}(177\,s, 400\,s) \Rightarrow v_{e,pop} > v_{e,ind}. \quad (6)$$

Again the difference between those two values is compared with the slope returned when the AIF_{pop}-based v_e is regressed onto the AIF_{ind}-based v_e.

3. Results

The acquisition of sagittal images allows for the axillary artery located in the FOV, permitting a robust identification of the artery. For each data set, there are approximately 12 slices ranging from 6 to 17 in which the artery is visible and approximately 300 voxels are selected manually. Four of the 20 data sets do not yield an acceptable AIF in that the AIFs measured manually do not return any voxels that satisfied the AIF search criteria which are used to capture the first pass or wash-out features. In the 16 useable data sets, 12 of these AIFs are derived from six patients who have been scanned both prior to and after one cycle of therapy, while the other four data sets come from four patients who have been scanned once. All analysis below is on these 16 data sets.

3.1. AIF tracking

The AIF detection approach allows for the identification of pixels located in the axillary artery area. It then removes the pixels which possess time courses that do not meet the above three AIF criteria. Figure 2 shows seven spatially adjacent slices with the detected artery (top row), the enlarged ROI with the manually detected arterial areas (blue) and the center points detected by the AIF tracking approach (red) superimposed, respectively. Note that the artery detected manually and automatically agrees well.

The detection algorithm is not sensitive to the parameters used in the criteria. More specifically, when the parameters are changed by $\pm 15\%$, the mean CC and CCC between the AIFs generated in this range are larger than 0.97 and the peak height of the AIF curves ranges from 5.03 to 6.11 mM (5.59 ± 0.43 mM), indicating the robustness of the algorithm and the relative insensitivity to assignment of the AIF criteria.
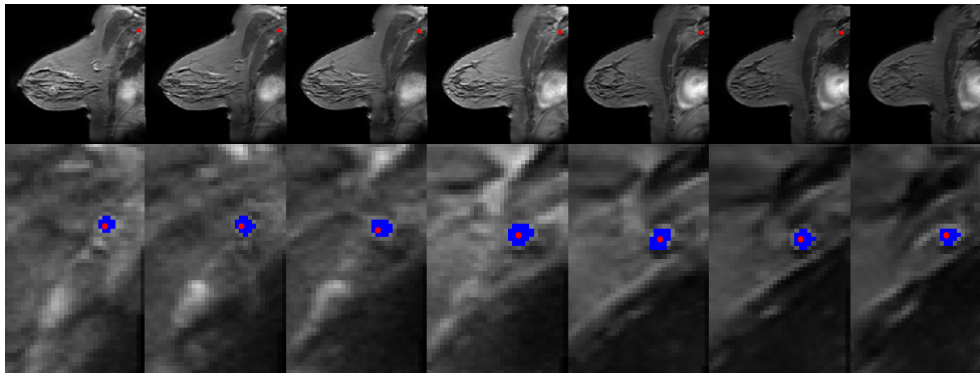
Figure 2. The figure displays seven successive slices with the detected artery (top row) and the zoomed-in ROIs with the manually detected arterial areas (blue) and the center points detected by the proposed AIF tracking approach (red) superimposed, respectively.

Table 1. The CCs and CCCs between the manually and automatically selected AIFs for the 16 data sets. Three sets of CC values were calculated: the first ~80 s (wash-in time), the last ~270 s (wash-out time) and the whole time course, respectively.

Data sets	Wash-in time		Wash-out time		Whole time course	
	CC	CCC	CC	CCC	CC	CCC
Mean ± 1.96 × SE	0.992 ± 0.0044	0.926 ± 0.039	0.967 ± 0.02	0.874 ± 0.058	0.992 ± 0.0031	0.955 ± 0.025

Approximately 7% of voxels manually segmented per data set meet the criteria. These voxels come from the center of the imaging slab, approximately from slice 6 to 15 of the 20 slice slab, indicating that the proposed criteria do not select the voxels most heavily influenced by unexcited spins flowing into the excited tissue section.

Figure 3 shows examples of five individual AIFs and the overall population-averaged AIF measured in different ways. Panels (a)–(e) display individual AIFs with the measured data points obtained by the manual method with and without applying for the criteria (dash-dotted line and dotted line, respectively) and the AIF returned by the AIF tracking method (solid line). Similarly, panel (f) displays the overall population-averaged data obtained manually with and without the criteria, as well as the AIF returned by the proposed AIF tracking method. In all cases, the AIF tracking method leads to an AIF similar to the one selected manually with the criteria. As also shown in the figure, without the criteria, the obtained AIF cannot display the typical AIF characteristics, such as rapid wash-in and wash-out. The AIF tracking method leads to the AIF curves that more closely resemble common AIF curves.

Computing the CC and CCC between the AIFs obtained manually with the criteria and by the proposed AIF tracking method allows for assessing the agreement between the two methods. Table 1 summarizes the three sets of CC and CCC computed: (1) over the first ~80 s wash-in period during the first five post-injection scans; (2) the last ~270 s wash-out time; (3) and the whole time course, for all 16 data sets. All three sets of mean CCs and CCCs between manual and automatic AIF estimation are larger than 0.85, indicating that the automatic detection algorithm and the manual method agree well.
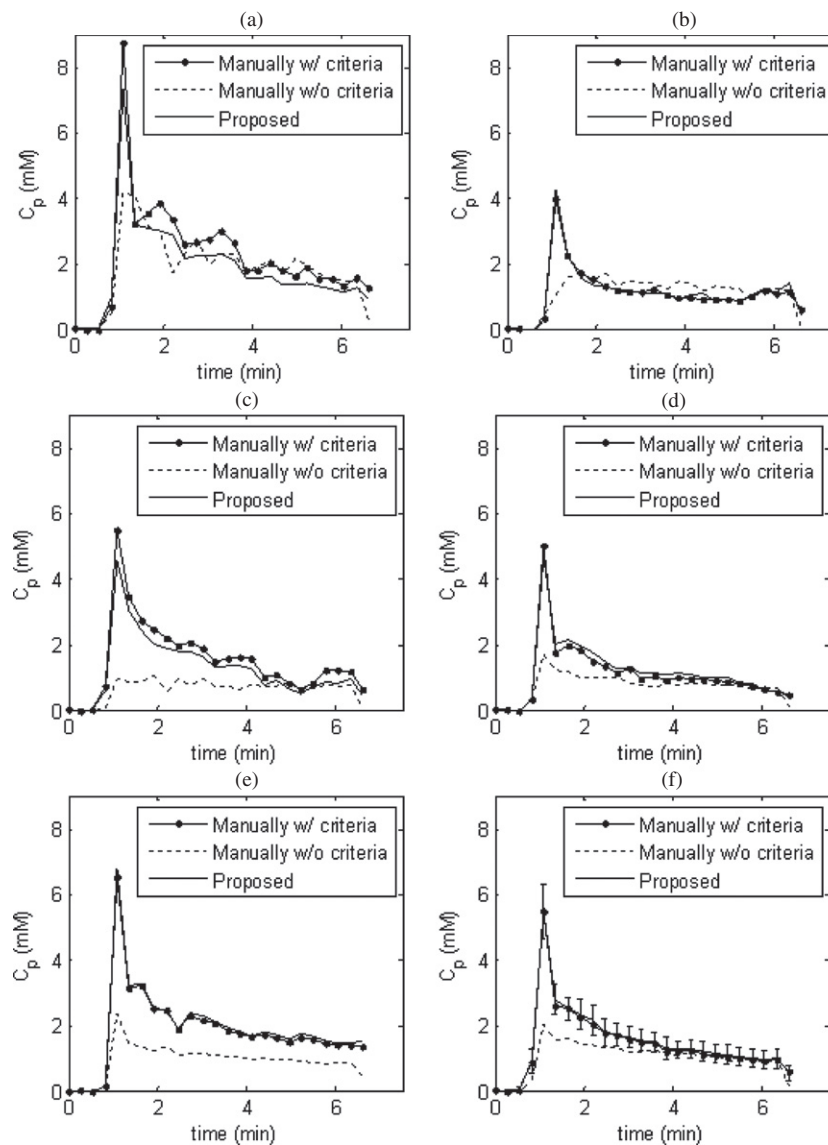
Figure 3. Panels (a)–(e) display individual AIFs with the measured data points obtained by the manual method with and without the criteria, and the AIF returned by the proposed method. Panel (f) displays the overall population-averaged data. The ($1.96 \times$ SE) bars of the AIFs obtained by the proposed method are also displayed in panel (f).

3.2. ROI analysis

As described above, the ROI-averaged signal time course from the tumor of each data set is examined. Each averaged time course is fit to the extended model (equation (3)) with either the AIF_{ind} or AIF_{pop} to extract the pharmacokinetic parameters. For each of the three parameters, 16 parameter pairs returned by AIF_{ind} and AIF_{pop} are generated and compared.
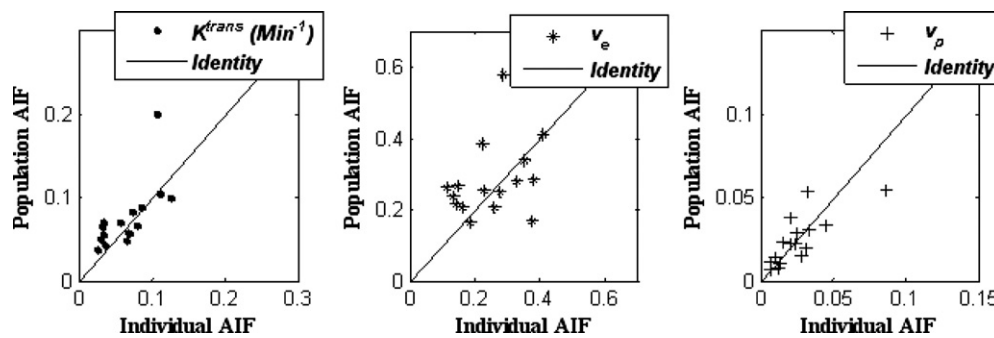
Figure 4. The parameters returned from the extended standard model, when the analyses use the AIF_{ind} and AIF_{pop}. Upon visual inspection, K^{trans} and v_p are closest to the identity line while v_e deviates the most.

Table 2. Results from the ROI-based comparison.

	CCC (CI)	Pearson (CI)	Slope (CI)	Intercept (CI)	Ratio (CI)
K^{trans}	0.65 (0.26–0.86)	0.69 (0.30–0.88)	0.84 (0.34–1.35)	0.02 (−0.02–0.06)	1.26 (1.02–1.5)
v_e	0.31 (−0.18–0.68)	0.33 (−0.2–0.71)	0.35 (−0.23–0.93)	0.19 (0.04–0.35)	1.26 (0.98–1.55)
v_p	0.74 (0.43–0.89)	0.77 (0.44–0.91)	0.59 (0.31–0.87)	0.01 (0.0006–0.02)	1.07 (0.85–1.29)

In figure 4, the *x*-axis is the value obtained using the AIF_{ind} and the *y*-axis is the value obtained using the AIF_{pop}, and each parameter pair is represented by a different symbol. The black line is the line of identity. If the AIF_{pop} yielded identical results to the AIF_{ind}, then all values in figure 4 would lie on the line of identity. Table 2 summarizes the statistical results. The CCC value of v_p is the highest (0.74), the CCC of K^{trans} is 0.63, while the CCC of v_e is 0.31. The lower confidence intervals of the CCC, CC and slope are less than 0.0 for v_e, indicating that the correlations are not significantly different from zero using the AIF_{ind} and AIF_{pop}. The large confidence interval is observed because the ROI analysis has a much smaller sample size, compared with the voxel analysis for each patient; that is, the voxel analysis has hundreds of voxels per patient, whereas the ROI only yields one value per patient. The obtained Pearson correlation coefficients of K^{trans} and v_p are 0.69 ($p = 0.003$) and 0.77 ($p = 0.000\,05$), respectively, which imply a relatively strong and significant linear correlation between the AIF_{ind} and AIF_{pop}. The results of the linear regression analysis show that K^{trans} is the parameter whose slope is closest to 1.0. The average ratio for v_p is 1.07, while K^{trans} and v_e have the same ratios (1.26) and similar confidence intervals (1.02–1.5 for K^{trans} and 0.98–1.55 for v_e) as presented in table 2.

3.3. Voxel analysis

In the second level of comparison, each voxel from the tumor ROI of each data set is fit to equations (2) and (3) to obtain paired parameters using both the AIF_{ind} and AIF_{pop}. Figure 5 displays parametric maps from one patient data set. The left column shows the maps overlaid on an anatomical image (derived from simply averaging the 25 dynamic scans) using the AIF_{ind}, while the middle column demonstrates the maps obtained using the AIF_{pop}. Each pair of parameters on this particular slice is plotted against each other in the right column. For this
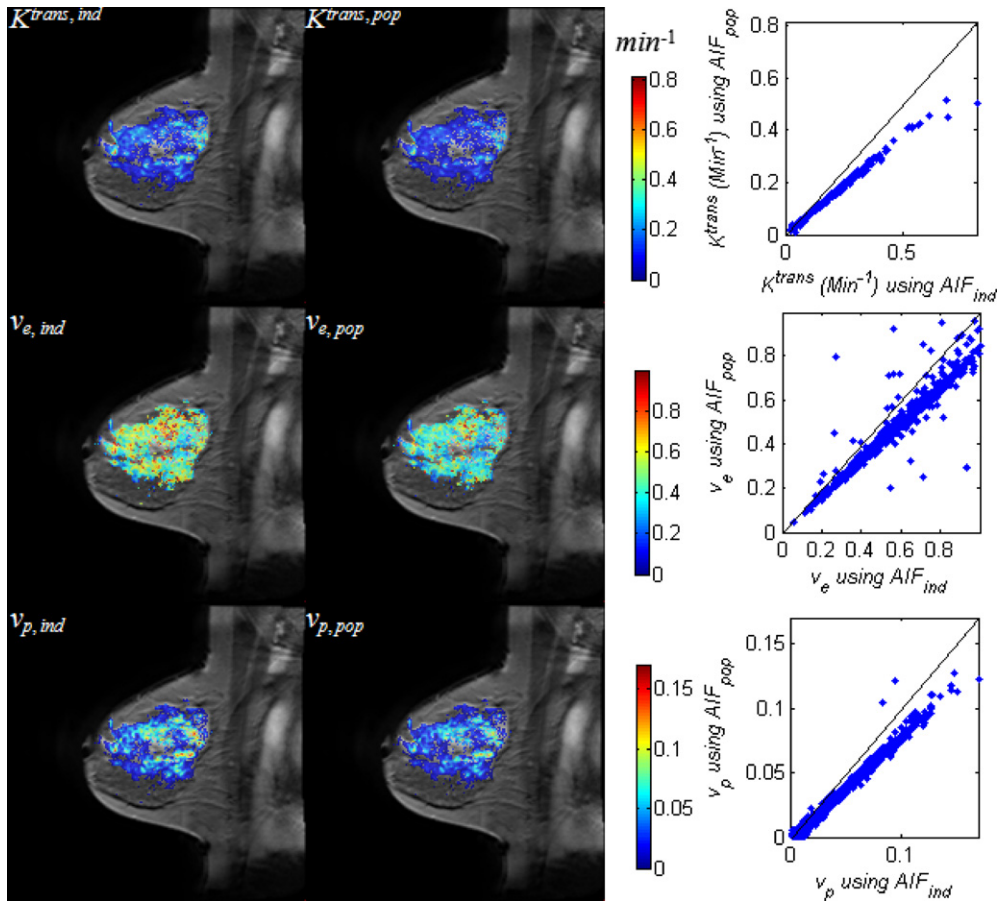
Figure 5. Parametric maps overlaid on a T_1-weighted image for patient 6. The left column depicts the three parameters using the AIF$_{ind}$ while the middle column shows the maps resulting from using the AIF$_{pop}$. Each parameter for each voxel on this slice is plotted with respect to its pair in the right column while the solid black line indicates the line of identity.

patient, the CC of both K^{trans} and v_p are larger than 0.99 ($p \ll 0.0001$) and the CC of v_e is 0.97 ($p \ll 0.0001$), indicating a strong correlation between the AIF$_{ind}$ and AIF$_{pop}$.

The CCC results are presented in figure 6. The CCC (x-axis) was plotted for each data set (y-axis) and the solid lines show the 95% CI boundaries for each value. The number on the right is the value of CCC. The AIF$_{ind}$ and AIF$_{pop}$ agree well on v_p, with the CCC evenly distributed within the range between 0.64 and 0.96. The CCCs are distributed between 0.36 and 0.96 for K^{trans}, while the CCCs are between 0.1 and 0.94 for v_e. Note that patient 5 is the source of the lower CCC value for both K^{trans} and v_e (0.36 and 0.1, respectively).

Table 3 presents the CC, linear regression and ratio results. The mean Pearson's correlations are high (CC > 0.85 and $p \ll 0.0001$) for all three parameters. The slopes of K^{trans} and v_p are 0.99 and 0.98, and their ratios are 0.95 and 1.04, respectively, showing good correlation between the AIF$_{pop}$ and AIF$_{ind}$, while the slope and ratio of v_e are 0.90 and 0.74, respectively.

Table 3. Results from the voxel-based analysis.

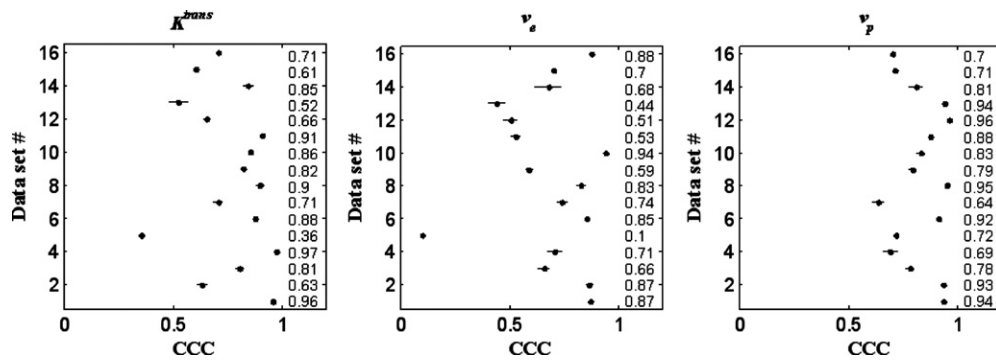| Data sets	CC			Slope			Intercept			Ratio		
	K^{trans}	v_e	v_p	K^{trans}	v_e	v_p	K^{trans}	v_e	v_p	K^{trans}	v_e	v_p
Mean $\pm$ 1.96 $\times$ SE	0.94 $\pm$ 0.034	0.89 $\pm$ 0.044	0.95 $\pm$ 0.017	0.99 $\pm$ 0.21	0.90 $\pm$ 0.18	0.98 $\pm$ 0.15	0.0025 $\pm$ 0.0042	0.029 $\pm$ 0.02	0.0008 $\pm$ 0.0017	0.95 $\pm$ 0.006	0.74 $\pm$ 0.01	1.04 $\pm$ 0.05

Figure 6. The CCC plots (*x*-axis) for each data set (*y*-axis). The solid line depicts the 95% CI for each point and the CCC values are listed in the column on the right side of the plot.
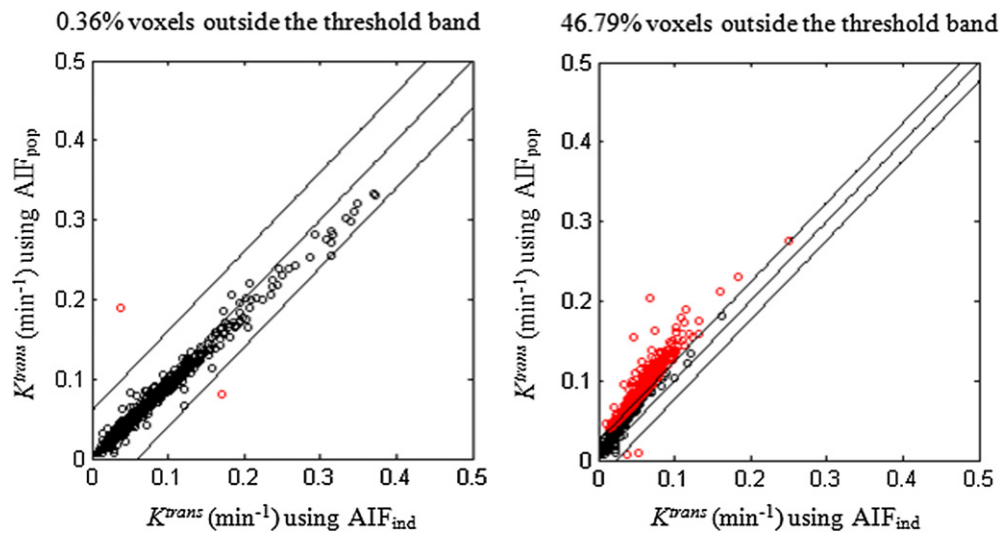

Figure 7. K^{trans} values of all tumor voxels using AIF_{ind} and AIF_{pop} and the $\pm 1.96 \times SD$ band are shown for data sets 10 and 12, respectively. Red data points represent voxels that have significant difference between AIF_{pop} and AIF_{ind}. The left panel shows the best case on K^{trans} in all data sets in which only 0.36% voxels fall outside the band, while the worst case is shown in the right panel (46.79% outside the band).

The standard deviation (SD) of the differences between parameters using the AIF_{pop} and AIF_{ind} is also calculated and differences that are larger than $1.96 \times SD$ are considered significant. This is based on the assumption that the SD estimated using the AIF_{pop} and AIF_{ind} is close to that estimated using repeated measures of the AIF_{ind}. An example is shown in figure 7, in which we plot K^{trans} values of all tumor voxels and the threshold bands (i.e. the $\pm 1.96 \times SD$) for data sets 10 and 12, respectively. Red data points represent voxels that have a significant difference between the AIF_{pop} and AIF_{ind}. The percentage of the voxels that fall outside the threshold is also calculated. This percentage quantifies how well the AIF_{pop} agrees with AIF_{ind}; a smaller percentage represents a better agreement. Figure 7 displays the best and worst cases on K^{trans} among all data sets, in which 0.36% and 46.79% voxels fall outside
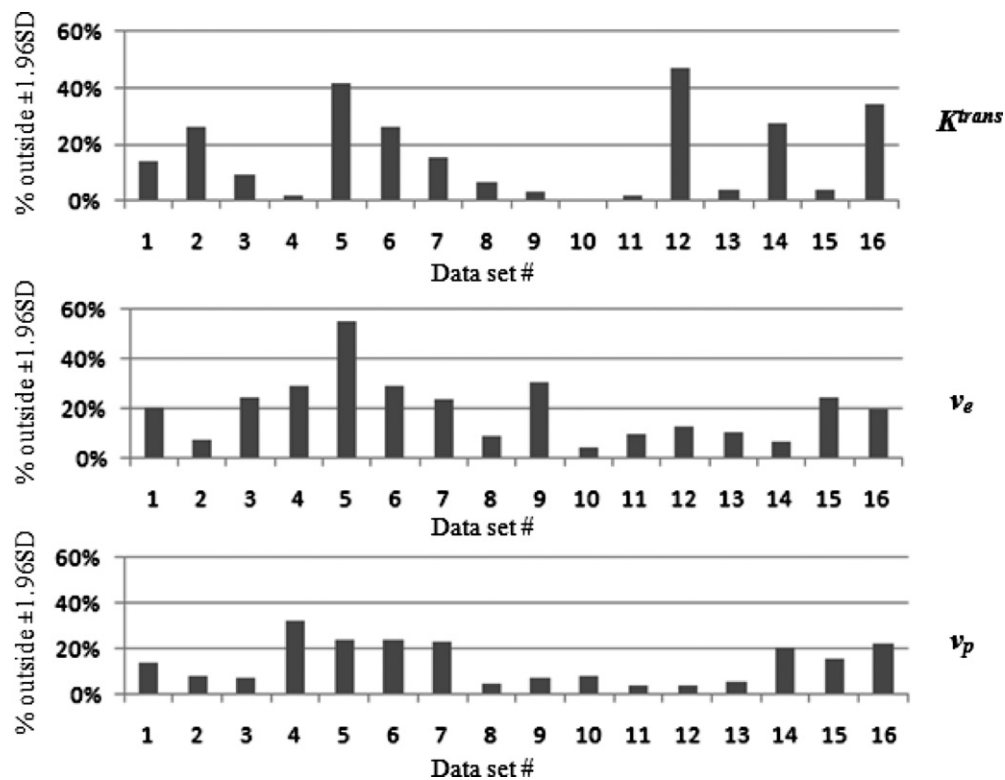
Figure 8. The percentages of the voxels (y-axis) that fall outside of the threshold $\pm 1.96 \times$ SD for each parameter and each data set (x-axis). Smaller percentages represent better agreement between the AIF_{pop} and AIF_{ind} analyses. More than 90% voxels fall inside the threshold bands in eight data sets on K^{trans} and v_p, while the majority of data sets have more than 10% voxels outside the band for v_e.

the threshold band, respectively. Figure 8 shows the percentages for each data set and each parameter. More than 90% of the voxels fall inside the threshold bands in eight data sets on K^{trans} and v_p, demonstrating good agreement between the AIF_{ind} and AIF_{pop}. The majority of the data sets have more than 10% voxels outside the threshold bands for v_e, showing a weaker agreement for this parameter between the AIF_{pop} and AIF_{ind}.

Figure 9 displays the results of plotting the differences in the AUC versus the slope of the regression line for parameters returned by the AIF_{pop} and AIF_{ind}. The left panel shows that as $AUC_{ind}(0 \text{ s}, 128 \text{ s}) - AUC_{pop}(0 \text{ s}, 128 \text{ s})$ increases, the magnitude of the regression slope between $K^{trans,pop}$ and $K^{trans,ind}$ increases. The middle and right panels depict similar results for v_p and v_e, respectively. As can be seen, there is a strong linear correlation between these values since the coefficient of determination, R^2, is 82% and 77%, respectively, indicating that the difference in K^{trans} and v_p values returned by the two AIFs is correlated with the differences in the initial shape of the population and individual AIFs. A strong linear relationship (R^2 is 72%) is displayed between the differences in the wash-out portion of AIF_{ind} and AIF_{pop} and the slope of the regression line between the v_e values returned by an AIF_{pop} and AIF_{ind} analysis. This also indicates that there is a correlation between the differences in v_e values returned by the two AIFs and the differences in the wash-out shape of the AIFs.
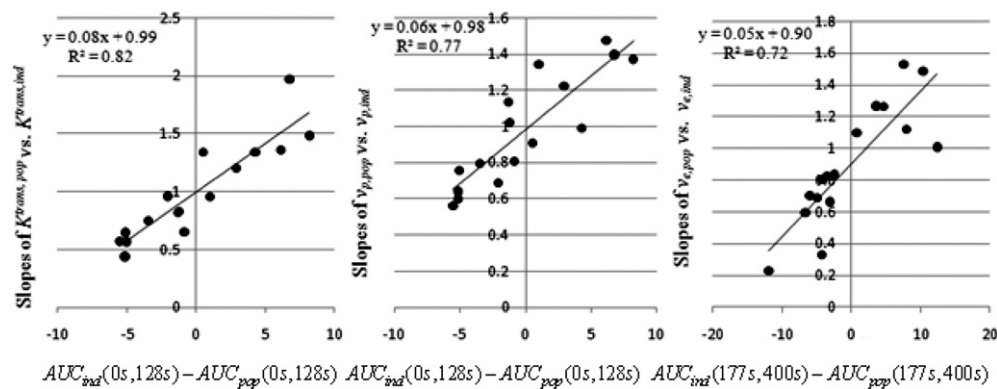
Figure 9. This figure displays the results of plotting the differences in the AUC versus the slope of the regression line for three parameters returned by the AIF_{pop} and AIF_{ind}. Panel a shows that as $\text{AUC}_{\text{ind}}(0\text{ s}, 128\text{ s}) - \text{AUC}_{\text{pop}}(0\text{ s}, 128\text{ s})$ increases, the magnitude of the regression slope between $K^{\text{trans,pop}}$ and $K^{\text{trans,ind}}$ increases. Panels (b) and (c) depict similar results for v_p and v_e. A strong linear correlation between these values indicates the differences in pharmacokinetic parameters returned by the population and individual AIFs are correlated with the differences in two AIFs.

It is also noted that the differences in the fits returned by the AIF_{pop} or AIF_{ind} are not statistically significant ($p > 0.5$) as measured by the standard chi-square test across all patients.

4. Discussion

Blood sampling may be considered the gold standard approach to measure the concentration of CA in the plasma. While it provides high accuracy in determining the CA concentration, it is a complicated and invasive procedure and therefore not appropriate for routine clinical use. In this study, an effective method is proposed to detect individual AIFs automatically once a seed point is determined within a sagittal slice containing the axillary artery. This method locates the voxels within the artery and selects the voxels that exhibit AIF characteristics. Voxels that do not exhibit these characteristics are not included in the AIF estimation. The reason why they do not exhibit those characteristics, though they appear to be physically located in the axillary artery, is partial volume effects; that is, a voxel may appear to be entirely within the artery, but it is actually a mixture of the blood pool, the vessel lumen and surrounding tissue. If such voxels are erroneously included in the calculation of the AIF, it would tend to decrease the value of $C_p(t)$ at each time point. This method is applied to 16 data sets and the obtained AIFs are compared with the AIFs generated manually. The high similarity between the two AIFs displays the reliability of the proposed AIF tracking method. Additionally, this method makes use of the fact that the area of the cross section of the artery stays approximately constant while its location shifts only slightly in consecutive sagittal slices, which simplifies the process. Hence, a weakness of this method is that it may not perform well in axial images since axial imaging makes detection of the artery substantially more difficult. Also, it is important to note that this study only demonstrates a high similarity between AIFs obtained by the proposed AIF tracking method and AIFs obtained manually, and it does not provide a validation to a gold-standard AIF measurement.

It is also important to determine whether or not a population AIF returns pharmacokinetic parameter values that are sufficiently similar to those returned by an individual AIF for at least

two reasons. In practice, it is very difficult to obtain a reliable AIF from each patient at each scanning session. Also, if a population AIF gives comparable results as an individual AIF, then high temporal resolution data would not necessarily be required since the blood CA kinetics are much fast than tissue CA kinetics, and therefore higher spatial resolution and/or SNR data could be acquired. Therefore, we performed ROI and voxel analyses of pharmacokinetic parameters obtained using the AIF_{pop} and AIF_{ind}. It is worth noting that although the AIF_{pop} is calculated from all of the individually measured AIF, the CCC method used in this study does not assume that they are independent, and therefore, the dependency between them does not affect the interpretation of our results. Our purpose is to determine if the population AIF is correlated with the individual AIF so that one can be used to replace the other.

The values of the CC for all three parameters in the voxel analysis show a stronger correlation between a population AIF and an individual AIF, compared with the CCC. This indicates that while a relatively large degree of linearity exists between the parameters, the AIF_{pop} will systematically over- or underestimate a given parameter for a given patient. We also note that the CCC of the data set 5 is consistently lower than those for the other patients. For this data set, there is only one voxel which satisfies the three criteria used in the AIF detection scheme. Thus, the AIF_{ind}, obtained from only one voxel, may be unreliable. This underscores the importance of assessing the feasibility of using a population AIF.

Overall, this study provides two options for the investigator: the AIF tracking method could be used on individual patients if a reliable population AIF is not available. Conversely, the K^{trans} and v_p parameters obtained from the AIF_{pop} and AIF_{ind} analyses showed good agreement, while v_e did not. Thus, if individual AIFs are not available and the parameters of interest are K^{trans} and v_p, a population AIF may suffice.

We also assess how the differences in early and late AUC values correlate to the pharmacokinetic parameters. It is hypothesized that if the wash-in AUC of the population AIF is greater than the wash-in AUC of the individual AIF, then the K^{trans} values returned from the individual AIF would be greater in magnitude than those returned from the population AIF analysis. Similarly, we hypothesized that if the wash-out AUC of the population AIF is greater than the wash-out AUC of the individual AIF, then the v_e value returned from the individual AIF would be greater in magnitude than those returned from the population AIF analysis. The results show that the difference in parameters returned by the two AIFs is strongly correlated with the difference in the shape of the AIFs.

One important limitation of this study is that the temporal resolution of 16 s is not optimal for AIF characterization; rather it represents a reasonable compromise between high temporal and high spatial resolution data that might actually be available in data from a clinical trial (see Ah-See *et al* 2008). The literature (Henderson *et al* 1998) has reported that a rapid injection combined with slow temporal sampling can lead to inaccurate and imprecise characterization of the pharmacokinetic parameters of interest; this is especially true when K^{trans} is large ($\sim$1.3 mL min^{-1} g^{-1}). While the K^{trans} values in our data set were not especially large, it is still absolutely true that our acquisition was not optimized for AIF characterization and this is a limitation of the study. However, it is still of great importance to compare the AIF_{ind}- and AIF_{pop}-based analyses and our effort does present a methodology for estimating AIFs in breast cancer patients, and performing a reasonable comparison of population and individual AIF-based DCE analysis.

Another limitation of the study is that the data is acquired at 3 T. There are known issues with B_1 inhomogeneities that can occur at this field strength (Kuhl 2007), and this can confound the estimation of baseline T_1 values measured through a multi-flip angle approach. To address this limitation for the AIFs, we assume a pre-contrast T_1 value of 1500 ms, as has been previously reported (Dagia and Ditchfield 2008). This limitation could still affect

signal-intensity time courses of both the tissue and the AIFs, leading to a reduction in the accuracy of the extracted pharmacokinetic parameters. This is not as much of an issue, though, because the errors would be present in both AIF_{ind} and AIF_{pop} analyses and would not bias the results toward one method or the other.

In our study, patient motion was minimal and, therefore, not a substantial source of error. In particular, for characterizing the AIF, motion did not present a concern because of the location of the artery in relation to the breast padding and support structure of the breast coil; that is, the upper-anterior portion of the chest is held firmly by gravity and patient weight against the support structure and does not move appreciably during the scan. Since the breasts hang pendant into the coil, they do have a greater chance of movement. With appropriate padding and support within the coil, motion in the tumor region of interest can be minimized as well. However, patient motion can still contribute to errors in the DCE analysis and future work should include applying nonrigid intensity-based registration algorithms (Rohde *et al* 2003, Rueckert *et al* 1999, Guo *et al* 2006) to retrospectively align data sets displaying substantial motion.

A final limitation that should be noted is that our study may not have acquired the necessary data to accurately estimate the entire range of v_e. The length of dynamic scanning time (i.e. how long one collects serial images after injection of the contrast agent) required to accurately estimate this parameter varies according to the values of K^{trans} and v_p. For example, Cao *et al* showed that, for a given v_e value, the lower the K^{trans} value, the longer the total acquisition time is required in order to accurately characterize the parameters (see figure 3 in Cao *et al* (2010)). In a clinical study, of course, a balance has to be struck between the optimal data collection method and patient comfort. The length of the dynamic scanning for this study of just under 7 min may not be long enough to accurately estimate v_e in voxels with low K^{trans}. This limitation may help to explain the lesser agreement between the population and individual AIF estimates of v_e.

In summary, a straightforward method has been introduced to obtain the AIF in breast DCE-MRI data that is obtained in the sagittal plane. A comparison is then performed between individually and population-based AIFs on the ROI and voxel analyses. K^{trans} and v_p show good absolute agreement (high CCC values) between AIF_{pop} and AIF_{ind}, whereas there is a week agreement on v_e. This may have important consequences for the design of breast cancer clinical trials that plan to incorporate quantitative DCE-MRI.

Acknowledgments

References

Ah-See M L *et al* 2008 Early changes in functional dynamic magnetic resonance imaging predict for pathologic response to neoadjuvant chemotherapy in primary breast cancer *Clin. Cancer Res.* **14** 6580–9

Cao Y, Li D, Shen Z and Normolle D 2010 Sensitivity of quantitative metrics derived from DCE MRI and a pharmacokinetic model to image quality and acquisition parameters *Acad. Radiol.* **17** 468–78

Checkley D, Tessier J J, Wedge S R, Dukes M, Kendrew J, Curry B, Middleton B and Waterton J C 2003 Dynamic contrast-enhanced MRI of vascular changes induced by the VEGF-signalling inhibitor ZD4190 in human tumour xenografts *Magn. Reson. Imaging* **21** 475–82

Chen J, Yao J and Thomasson D 2008 Automatic determination of arterial input function for dynamic contrast enhanced MRI in tumor assessment *Med. Image Comput. Comput. Assist. Interv.* **11** 594–601

Cheng H L 2008 Investigation and optimization of parameter accuracy in dynamic contrast-enhanced MRI *J. Magn. Reson. Imaging* **28** 736–43

Choyke P L, Dwyer A J and Knopp M V 2003 Functional tumor imaging with dynamic contrast-enhanced magnetic resonance imaging *J. Magn. Reson. Imaging* **17** 509–20

Dagia C and Ditchfield M 2008 3T MRI in paediatrics: challenges and clinical applications *Eur. J. Radiol.* **68** 309–19

Delille J P, Slanetz P J, Yeh E D, Halpern E F, Kopans D B and Garrido L 2003 Invasive ductal breast carcinoma response to neoadjuvant chemotherapy: noninvasive monitoring with functional MR imaging pilot study *Radiology* **228** 63–9

Guo Y, Sivaramakrishna R, Lu C C, Suri J S and Laxminarayan S 2006 Breast image registration techniques: a survey *Med. Biol. Eng. Comput.* **44** 15–26

Hamstra D A *et al* 2005 Evaluation of the functional diffusion map as an early biomarker of time-to-progression and overall survival in high-grade glioma *Proc. Natl. Acad. Sci. USA* **102** 16759–64

Hayes C, Padhani A R and Leach M O 2002 Assessing changes in tumour vascular function using dynamic contrast-enhanced magnetic resonance imaging *NMR Biomed.* **15** 154–63

Henderson E, Rutt B K and Lee T Y 1998 Temporal sampling requirements for the tracer kinetics modeling of breast disease *Magn. Reson. Imaging* **16** 1057–73

Kuhl C K 2007 Breast MR imaging at 3T *Magn. Reson. Imaging Clin. North Am.* **15** 315–20 vi

Landis C S, Li X, Telang F W, Coderre J A, Micca P L, Rooney W D, Latour L L, Vetek G, Palyka I and Springer C S 2000 Determination of the MRI contrast agent concentration time course in vivo following bolus injection: effect of equilibrium transcytolemmal water exchange *Magn. Reson. Med.* **44** 563–74

Lin L I 1989 A concordance correlation coefficient to evaluate reproducibility *Biometrics* **45** 255–68

Martincich L *et al* 2004 Monitoring response to primary chemotherapy in breast cancer using dynamic contrast-enhanced magnetic resonance imaging *Breast Cancer Res. Treat.* **83** 67–76

McGrath D M, Bradley D P, Tessier J L, Lacey T, Taylor C J and Parker G J M 2009 Comparison of model-based arterial input functions for dynamic contrast-enhanced MRI in tumor bearing rats *Magn. Reson. Med.* **61** 1173–84

Mouridsen K, Christensen S, Gyldensted L and Ostergaard L 2006 Automatic selection of arterial input function using cluster analysis *Magn. Reson. Med.* **55** 524–31

Nagashima T, Sakakibara M, Nakamura R, Arai M, Kadowaki M, Kazama T, Nakatani Y, Koda K and Miyazaki M 2006 Dynamic enhanced MRI predicts chemosensitivity in breast cancer patients *Eur. J. Radiol.* **60** 270–4

Parker G J, Jackson A, Waterton J C and Buckley D L 2003 Automated arterial input function extraction for T1-Weighted DCE-MRI *Proc. Intl Soc. Mag. Reson. Med. (ISMRM) (Toronto, Canada)* p 1264

Parker G J M, Roberts C, Macdonald A, Buonaccorsi G A, Cheung S, Buckley D L, Jackson A, Watson Y, Davies K and Jayson G C 2006 Experimentally-derived functional form for a population-averaged high-temporal-resolution arterial input function for dynamic contrast-enhanced MRI *Magn. Reson. Med.* **56** 993–1000

Rijpkema M, Kaanders J H, Joosten F B, van der Kogel A J and Heerschap A 2001 Method for quantitative mapping of dynamic MRI contrast agent uptake in human tumors *J. Magn. Reson. Imaging* **14** 457–63

Rohde G K, Aldroubi A and Dawant B M 2003 The adaptive bases algorithm for intensity-based nonrigid image registration *IEEE Trans. Med. Imaging* **22** 1470–9

Rueckert D, Sonoda L I, Hayes C, Hill D L, Leach M O and Hawkes D J 1999 Nonrigid registration using free-form deformations: application to breast MR images *IEEE Trans. Med. Imaging* **18** 712–21

Schabel M C, Morrell G R, Oh K Y, Walczak C A, Barlow R B and Neumayer L A 2010 Pharmacokinetic mapping for lesion classification in dynamic breast MRI *J. Magn. Reson. Imaging* **31** 1371–8

Wang Y, Huang W, Panicek D A, Schwartz L H and Koutcher J A 2008 Feasibility of using limited-population-based arterial input function for pharmacokinetic modeling of osteosarcoma dynamic contrast-enhanced MRI data *Magn. Reson. Med.* **59** 1183–9

Yankeelov T E and Gore J C 2007 Dynamic contrast enhanced magnetic resonance imaging in oncology: theory, data acquisition, analysis, and examples *Curr. Med. Imaging Rev.* **3** 91–107

Yankeelov T E *et al* 2007 Integration of quantitative DCE-MRI and ADC mapping to monitor treatment response in human breast cancer: initial results *Magn. Reson. Imaging* **25** 1–13

Yankeelov T E, Rooney W D, Huang W, Dyke J P, Li X, Tudorica A, Lee J H, Koutcher J A and Springer C S Jr 2005 Evidence for shutter-speed variation in CR bolus-tracking studies of human pathology *NMR Biomed.* **18** 173–85

Yankeelov T E, Rooney W D, Li X and Springer C S 2003 Variation of the relaxographic 'shutter-speed' for transcytolemmal water exchange affects the CR bolus-tracking curve shape *Magn. Reson. Med.* **50** 1151–69